Original Research

Specific Absorption Rate Studies of the Parallel Transmission of Inner-Volume Excitations at 7T

Adam C. Zelinski, PhD,[1]* Leonardo M. Angelone, PhD,[2] Vivek K. Goyal, PhD,[1] Giorgio Bonmassar, PhD,[2] Elfar Adalsteinsson, PhD,[1,3] and Lawrence L. Wald, PhD[2,3]

Purpose: To investigate the behavior of whole-head and local specific absorption rate (SAR) as a function of trajectory acceleration factor and target excitation pattern due to the parallel transmission (pTX) of spatially tailored excitations at 7T.

Materials and Methods: Finite-difference time domain (FDTD) simulations in a multitissue head model were used to obtain B_1^+ and electric field maps of an eight-channel transmit head array. Local and average SAR produced by 2D-spiral-trajectory excitations were examined as a function of trajectory acceleration factor, R, and a variety of target excitation parameters when pTX pulses are designed for constant root-mean-square excitation pattern error.

Results: Mean and local SAR grow quadratically with flip angle and more than quadratically with R, but the ratio of local to mean SAR is not monotonic with R. SAR varies greatly with target position, exhibiting different behaviors as a function of target shape and size for small and large R. For example, exciting large regions produces less SAR than exciting small ones for $R \geq 4$, but the opposite trend occurs when $R < 4$. Furthermore, smoother and symmetric patterns produce lower SAR.

Conclusion: Mean and local SAR vary by orders of magnitude depending on acceleration factor and excitation pattern, often exhibiting complex, nonintuitive behavior. To ensure safety compliance, it seems that model-based validation of individual target patterns and corresponding pTX pulses is necessary.

PARALLEL TRANSMISSION (pTX) of radiofrequency (RF) pulses in the presence of two-dimensional (2D) and three-dimensional (3D) gradient trajectories (1–5) offers a flexible means for volume excitation (6) and the mitigation of main field (B_0) and B_1^+ inhomogeneity (7), the latter of which is particularly prevalent at high field in the body (8) and brain (9,10) due to wavelength interference (9,10) and tissue-conductive RF-amplitude attenuation (11). Parallel transmission systems are able to accomplish these tasks because unlike standard single-channel systems, their RF excitation coils consist of multiple independent transmission elements with unique spatial profiles, all of which may be modulated and superimposed to nearly arbitrarily tailor the magnitude and phase of the transverse magnetization (12) across a chosen field of excitation (FOX) (subject to gradient and RF hardware constraints).

Parallel transmission systems are promising because they enable one to reduce the duration of an RF pulse even after one has exhausted the ability to do so by increasing the amplitude and slew rates of the system's gradient coils. Namely, when using a parallel excitation system rather than a conventional single-channel transmit array, one may significantly undersample the excitation k-space trajectory, reducing the distance traveled in k-space, in turn reducing the duration of the corresponding RF pulse (1–5). The reduction of pulse length is important given the lengthy durations of typical 2D and 3D spatially tailored excitation pulses and gradient hardware limitations. The ability to "accelerate" in the k-space domain arises due to the extra degrees of freedom provided by the system's multiple transmit elements, analogous to readout-side acceleration where multiple reception channels allow one to undersample readout k-space and reduce readout time (13,14).

Unfortunately, high specific absorption rate (SAR)—defined as the average energy deposition in a region of a certain mass over an extended period of time due to the

application of an excitation pulse—is a major concern in the parallel transmission of spatially tailored multidimensional excitation pulses, especially the potential for a relatively high ratio of local SAR to average SAR. When multiple transmit channels are simultaneously employed the local electric fields generated by each channel undergo local superposition and thus local extremes in electric field magnitude may arise (5), causing spikes in local SAR ("hot spots"). Additionally, using pTX to accelerate a given k-space trajectory and reduce pulse duration has the detrimental effect of increasing peak pulse power and thus SAR (15–17). For example, a conventional hard excitation pulse requires a peak power increase by a factor of C as its duration is shortened by the same factor, causing global SAR to increase by a factor of C^2. Furthermore, even when the repetition time (TR) of the pulse is kept constant such that total RF duty cycle decreases by a factor of C, SAR still increases linearly with C (18).

In this article we seek to investigate the above concerns and test if global and local SAR obey intuitive scaling rules as a function of excitation k-space trajectory acceleration factor and the parameters of an inner-volume excitation pattern excited by 2D spatially tailored RF excitation pulses. Our goal is to give pulse designers, coil array engineers, and RF safety researchers insight into the SAR characteristics of a high-field pTX system. Specifically, we study whole-head and maximum local 1 gram (1g) and 10 gram (10g) SAR in a multitissue head model during constant-fidelity excitation of 2D boxes. Box-shaped excitations are useful because they allow one to exclude moving tissues from a volume undergoing imaging (6) and also permit reduced field-of-view (FOV) imaging, which improves temporal resolution without compromising spatial resolution (19). Such excitations have applications to echo-volumnar imaging (20,21) as well as perfusion territory mapping via arterial spin labeling (22).

The fidelity of each box-shaped excitation is kept constant as measured by normalized root-mean-square error (NRMSE) with respect to a target pattern. The simulations are based on an eight-channel parallel transmission system at 7T; this field strength is chosen because many researchers are focusing on using pTX to mitigate B_1^+ inhomogeneity occurring at 7T. Local 1g and 10g SAR are studied in addition to whole-head mean SAR because these correspond to limits specified by the Food and Drug Administration (FDA) (23) and the International Electrotechnical Commission (IEC) (24,25), and will permit observation of local SAR hot spots.

The study uses finite-difference time domain (FDTD) simulations (26) in a multitissue high-resolution head model as described by Angelone et al. (27), obtaining electric and B_1^+ fields generated by each array element when its corresponding channel is driven by a unit current, as described by Angelone et al. (28). The B_1^+ maps are then used to design a variety of pTX box-shaped excitations, the latter of which are validated with Bloch-equation simulations. Finally, the electric field maps are used to calculate whole-head and maximum local 1g and 10g SAR due to each pTX pulse as a function of target flip angle, position, size, smoothness,

and orientation, as well as spiral trajectory undersampling (acceleration) factor, R. The results demonstrate a wide range of SAR values that arise due to tailored excitations that produce similar spatial patterns. These data, together with the nonintuitive behavior SAR exhibits as a function of the excitation parameters, suggests that explicit SAR calculations will likely be needed on a per-pulse basis, even for relatively minor variations in RF pulse properties, in order to ensure that local SAR values meet regulatory criteria.

MATERIALS AND METHODS

Human Head and Eight-Channel Parallel Transmit Array Model

Head Model

SAR characteristics of excitation pulses transmitted through an eight-channel head array are calculated in a high-resolution ($1 \times 1 \times 2$ mm^3) 29-tissue human head model, the latter of which is obtained via segmentation of anatomical MRI data. Each of the tissues in the model is assigned a density, ρ (kg/m^3), and electrical conductivity, σ (S/m), using Federal Communications Commission data available at www.fcc.gov/fcc-bin/dielec.sh. Overall, the model consists of $\approx$2.3 million Yee cells (29).

Excitation Array

The pTX system is modeled by placing eight copper circular loop elements at 45° increments along a 25-cm-diameter cylindrical surface, the latter of which is centered on the head, as described by Angelone et al (28). Each loop element is overlapped to null mutual inductance with its neighbors and has a diameter of 15 cm, a trace width of 1 cm, and an input resistance of 50Ω.

Electromagnetic Field Simulations and B_1^+ Field Map Generation

Overview

Electric and B_1^+ fields produced in the head by each individual transmit channel are needed in order to design and calculate the SAR of pTX excitation pulses. We obtain these via 300-MHz FDTD simulations (XFDTD software, REMCOM, State College, PA), and then evaluate the SAR of any given excitation by superimposing modulated versions of these electric fields (5,18,30,31), avoiding the computationally intractable scenario of FDTD-simulating each of the 200+ pTX excitations evaluated in this study.

FDTD Simulation

For $p = 1, \ldots, 8$, we drive the pth transmit channel of the eight-channel array with a 1-ampere peak-to-peak 300-MHz sinusoid, leave all other channels dormant, and use the FDTD method to obtain steady-state electric fields per ampere of input to the pth channel, $\mathbf{E}_p(\mathbf{r}) = [E_{p,x}(\mathbf{r}), E_{p,y}(\mathbf{r}), E_{p,z}(\mathbf{r})]^T$ (V/m/ampere), and magnetic fields, $\mathbf{B}_p(\mathbf{r}) = [B_{p,x}(\mathbf{r}), B_{p,y}(\mathbf{r}), B_{p,z}(\mathbf{r})]^T$ (T/ampere), generated at each of the $\approx$2.3 million spatial locations $\mathbf{r} = [x,$
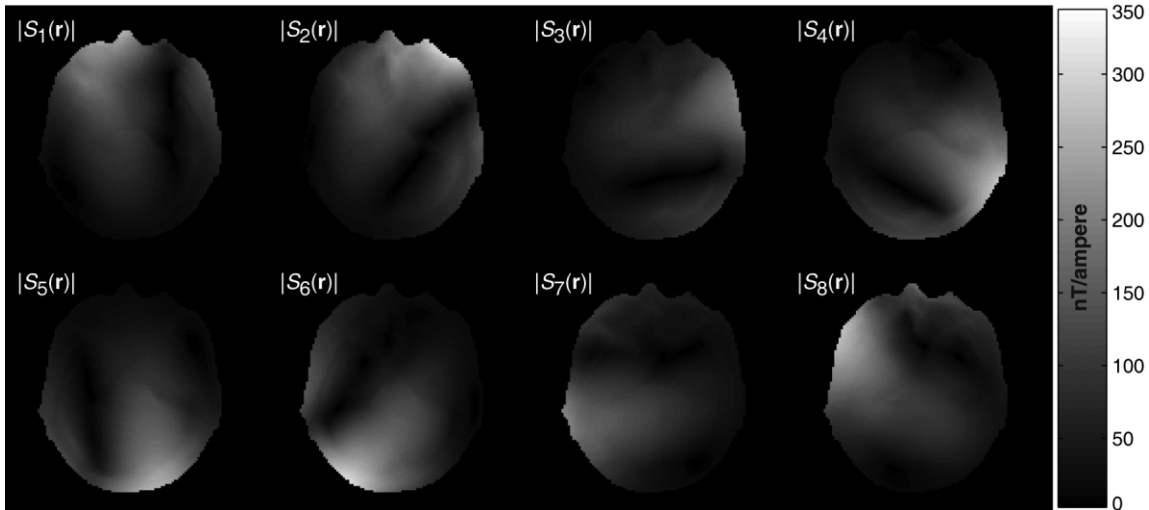
Figure 1. Quantitative B_1^+ maps (nT/ampere) of the center transverse slice of the head derived from FDTD-simulated fields. Each map exhibits severe inhomogeneity. $S_p(\mathbf{r})$ is the B_1^+ field that arises when channel p is driven with a 1-ampere peak-to-peak 300-MHz sinusoid.

y, $z]^T$ in the head. The use of current sources allows us to accurately approximate the simultaneous-drive behavior of the array by simply superimposing the field maps of individual channels (30).

B_1^+ Maps

The B_1^+ field that arises when channel p is driven by the unit ampere input, denoted $S_p(\mathbf{r})$, is derived at all locations $\mathbf{r}$ as follows (32):

$$S_p(\mathbf{r}) = \frac{1}{2}\{B_{p,x}(\mathbf{r}) + jB_{p,y}(\mathbf{r})\} \quad \text{(T/ampere)}. \qquad [1]$$

where "S_p" is used (rather than "$B_{1,p}^+$") to keep upcoming formulations concise. Figure 1 depicts the magnitude of the eight B_1^+ field maps obtained via Eq. [1]; each is inhomogeneous.

Parallel Excitation RF Pulse Design

Overview

We now describe one way to design a set of P RF pulse shapes to concurrently play through the P elements of a P-channel parallel transmission array in order to generate a user-defined target excitation, $d(\mathbf{r})$. Note that "pTX pulse" will be used as shorthand for "a set of P concurrently transmitted RF pulse shapes that yields a box-shaped excitation." To begin, we will apply the linear formalism of Ref. (33) to reduce the design problem to that of solving a linear system. Assume for now that the gradient waveforms, $\mathbf{G}(t) = [G_x(t),\ G_y(t),\ G_z(t)]^T$, are fixed (ie, the k-space trajectory, $\mathbf{k}(t) = [k_x(t),\ k_y(t),\ k_z(t)]^T$, is predetermined) and that each of the P channel's B_1^+ profiles are known.

Design Constants

For all upcoming simulations we design pTX pulses that form approximations of a 2D box-shaped inner-volume target in the center transverse slice of the head; the desired excitation has zero-degree flip angle at spatial locations outside of the box, a positive flip angle inside the box, and zero phase everywhere. The FOX is the center transverse slice of the head. The k-space trajectories are 2D spirals that are radially under-sampled (accelerated) by a factor of R relative to a 25.6 cm FOV, where $R = 1, 2, ..., 8$. Based on this definition, the $R = 1$ spiral is simply a conventional Nyquist-sampled spiral. The gradients are always constrained to amplitude and slew rates of 30 mT/m and 300 T/m/s, such that the $R = 1, ..., 8$ spiral trajectories have durations of 6.8 msec, 3.47 msec, 2.36 msec, 1.81 msec, 1.48 msec, 1.26 msec, 1.11 msec, and 0.99 msec.

Linearization

We first apply the small-tip-angle approximation (12) to the Bloch equation (34), yielding:

$$m(\mathbf{r}) = j\gamma M_0 \sum_{p=1}^{P} S_p(\mathbf{r}) \int_0^L a_p(t)e^{j\mathbf{r}\cdot\mathbf{k}(t)}dt, \qquad [2]$$

where m is the (approximate) complex-valued transverse magnetization (rad) arising due to the transmission of the P RF pulse shapes (i.e., one pTX pulse) in the presence of the gradients, γ the gyromagnetic ratio (rad/T/sec), M_0 the steady-state magnetization, $S_p(\mathbf{r})$ the B_1^+ profile of channel p (T/ampere), $a_p(t)$ the RF pulse shape played along the pth channel (amperes), L the duration of each of the P RF pulse shapes (sec), and $\mathbf{k}(t) = -\gamma \int_t^L \mathbf{G}(\tau)d\tau$ (33).

Discretization

We now discretize Eq. [2] by sampling space at locations $\mathbf{r}_1, ..., \mathbf{r}_{Ns}$ within the user-defined FOX and sampling

time at $t_1, ..., t_{Nt} \in [0, L]$; the t_i are spaced uniformly by Δ_t. This yields:

$$\mathbf{m} = \mathbf{S}_1\mathbf{F}\mathbf{a}_1 + \cdots + \mathbf{S}_P\mathbf{F}\mathbf{a}_P = [\mathbf{S}_1\mathbf{F}\cdots\mathbf{S}_P\mathbf{F}]\begin{bmatrix} \mathbf{a}_1 \\ \vdots \\ \mathbf{a}_P \end{bmatrix} = \mathbf{A}_{\text{tot}}\mathbf{a}_{\text{tot}},$$

[3]

where $\mathbf{m}$ is an N_s-element vector of samples of $m(\mathbf{r})$, $\mathbf{S}_p$ an $N_s \times N_s$ diagonal matrix containing samples of $S_p(\mathbf{r})$ taken within the FOX, and $\mathbf{F}$ an $N_s \times N_t$ matrix where $\mathbf{F}(m,n) = j\gamma M_0\Delta_t e^{j\mathbf{r}_m \cdot \mathbf{k}(t_n)}$; $\mathbf{F}$ brings energy in k-space into the spatial domain at the N_s locations where each transmit profile and the resulting magnetization are sampled. Finally, each $\mathbf{a}_p$ is an N_t-element vector of current samples of $a_p(t)$. By sampling $\mathbf{r}$ only within the FOX, the system of equations is blind to the rest of the FOV; this avoids imposing needless spatial constraints on the system. Note that as a spiral trajectory is accelerated, fewer points in k-space are traversed and degrees of freedom in k-space are lost. The number of spatial-domain constraints, however, remains constant, which means that the number of columns of $\mathbf{A}_{\text{tot}}$ decreases with R while the number of rows remains constant, causing the overall system in Eq. [3] to become increasingly overdetermined with R.

pTX Pulse Design

To excite a desired pattern, $d(\mathbf{r})$, P pulse shapes are needed. To generate these pulse shapes we first determine B_1^+ maps for each of the P channels and then decide on a k-space trajectory, which lets us generate $\mathbf{S}_p$, $\mathbf{F}$, and $\mathbf{A}_{\text{tot}}$ in Eq. [3]. We then sample $d(\mathbf{r})$ at $\mathbf{r}_1, ..., \mathbf{r}_{Ns}$ and stack these N_s samples into the vector $\mathbf{d}$. At this point, one way to generate a set of pulse shapes that (approximately) produce the desired excitation is to solve:

$$\min_{\mathbf{a}_{\text{tot}}} \{\|\mathbf{d} - \mathbf{A}_{\text{tot}}\mathbf{a}_{\text{tot}}\|_2^2 + \lambda\|\mathbf{a}_{\text{tot}}\|_2^2\}$$

[4]

for $\mathbf{a}_{\text{tot}}$. In practice, setting λ to a small nonnegative value and solving Eq. [4] results in a reasonably conditioned solution that produces an excitation close (in the L_2 sense) to the one desired (33). After solving Eq. [4], we extract samples of each $a_p(t)$ waveform from $\mathbf{a}_{\text{tot}}$ and play these waveforms on an actual system (or a Bloch-equation simulator) to produce an excitation that resembles the desired one (3). Unfortunately, Eq. [4] does not let us allocate and fix the residual error between the resulting and desired excitation across different spatial regions. For example, for box-shaped excitations, designers are willing to tolerate larger errors outside of the box but require within-box error to be small. Equation [4] gives us only one variable, λ, with which to influence overall error, and we are thus unable to design pTX pulses that achieve both a chosen in-box error and a chosen overall (or out-of-box) error.

To circumvent this problem, we pose a novel algorithm that designs a pTX pulse that yields an excitation with both a desired in-box error and a desired overall error. First, we arrange N_{in} within-box samples of $d(\mathbf{r})$

into $\mathbf{d}_{\text{in}}$, and N_{out} out-of-box samples into $\mathbf{d}_{\text{out}}$ (where $N_{\text{in}} + N_{\text{out}} = N_s$), and then set $\mathbf{d} = [\mathbf{d}_{\text{in}}^T, \mathbf{d}_{\text{out}}^T]^T$. Likewise, we structure $\mathbf{A}_{\text{in}}$ and $\mathbf{A}_{\text{out}}$ such that $\mathbf{A}_{\text{tot}} = [\mathbf{A}_{\text{in}}^T, \mathbf{A}_{\text{out}}^T]^T$. These steps are analogous to those above that lead to Eq. [4]. With these new variables, we solve:

$$\min_{\mathbf{a}_{\text{tot}}} \{\|\mathbf{W}(\mathbf{d} - \mathbf{A}_{\text{tot}}\mathbf{a}_{\text{tot}})\|_2^2 + \lambda\|\mathbf{a}_{\text{tot}}\|_2^2\},$$

[5]

where $\mathbf{W}$ is an $N_s \times N_s$ diagonal matrix such that $\mathbf{W}(n,n) = \alpha$ if $n \in [1, ..., N_{\text{in}}]$ and unity otherwise. Thus, $\mathbf{W}$ weights within-box and out-of-box errors by α and unity, respectively. Equation [5] has two variables, α and λ, and we are now able to control both in-box error and overall error while still ensuring a well-conditioned solution.

In this study, within-box and overall NRMSE are used as fidelity metrics and expressed as percentages. In-box NRMSE, ϵ_1, is defined as $100 \cdot (\|\mathbf{d}_{\text{in}} - \mathbf{A}_{\text{in}}\mathbf{a}_{\text{tot}}\|_2/\|\mathbf{d}_{\text{in}}\|_2)$, whereas overall NRMSE, ϵ_{tot}, is defined as $100 \cdot (\|\mathbf{d} - \mathbf{A}_{\text{tot}}\mathbf{a}_{\text{tot}}\|_2/\|\mathbf{d}\|_2)$. Whenever we design a pTX pulse, we first decide on a desired in-box error and overall error, denoted $\epsilon_{1,\text{des}}$ and $\epsilon_{\text{tot,des}}$. We then iteratively search over (α, λ), repeatedly solving Eq. [5] until a solution $\mathbf{a}_{\text{tot}}$ is found such that the resulting ϵ_1 and ϵ_{tot} are close to $\epsilon_{1,\text{des}}$ and $\epsilon_{\text{tot,des}}$. Finally, we simulate the waveform samples in $\mathbf{a}_{\text{tot}}$ and compare the simulated excitation to the desired one, ensuring that ϵ_1 and ϵ_{tot} remain close to $\epsilon_{1,\text{des}}$ and $\epsilon_{\text{tot,des}}$. Overall, this approach lets us design a variety of pTX pulses across different scenarios while guaranteeing that every excitation has essentially identical in-box and overall error.

Whole-Head and Local Specific Absorption Rate Calculations

Overview

After designing P pulse shapes to produce a desired excitation, we must determine the global and local SAR they produce in the head model. At this point, we know N_t time samples of each pulse shape spaced uniformly in time by Δ_t, ie, for $p = 1, ..., P$, we have $[a_p(n\Delta_t) \mid n \in [0, 1, N_t - 1]]$. Recall from Eq. [2] that L is *overall* pTX pulse duration and thus will exceed $(N_t - 1)\Delta_t$ if the duty cycle is set to less than 100% (see end of subsection).

SAR per Voxel

We first calculate SAR (W/kg) at each location $\mathbf{r}$ by superimposing the electric field produced by each transmit channel due to each time sample in the RF pulse shape and then time averaging the net field's squared magnitude over the pTX pulse duration and weighting by the conductivity and density of that location. Formally,

$$\text{SAR}(\mathbf{r})$$

$$= \frac{\sigma(\mathbf{r})}{2\rho(\mathbf{r})}\frac{1}{L}\int_0^L \|\mathbf{E}(\mathbf{r},t)\|_2^2 dt \cong \frac{\sigma(\mathbf{r})}{2L\rho(\mathbf{r})}\Delta_t\sum_{n=0}^{N_t-1}\|\mathbf{E}(\mathbf{r},n\Delta_t)\|_2^2, \quad [6]$$

where $\mathbf{E}(\mathbf{r}, t)$ is the superposition of the electric fields generated by each of the channels scaled by the waveform samples transmitted at each time instant (5), ie:

$$\mathbf{E}(\mathbf{r},t) = \sum_{p=1}^{P} a_p(t)\mathbf{E}_p(\mathbf{r}). \qquad [7]$$

Recall that each $\mathbf{E}_p(\mathbf{r})$ is the 3D electric field (obtained via FDTD simulation) that arises when channel p is driven by a unit ampere waveform, and that ρ and σ are given by the head model.

Whole-Head and Local N-gram SAR

Having obtained SAR($\mathbf{r}$) for all $\mathbf{r}$ in the head, whole-head global SAR is obtained by averaging the SAR($\mathbf{r}$) values. Likewise, N-gram SAR at each $\mathbf{r}$ is obtained by finding an N-gram cube around each $\mathbf{r}$ and then averaging SAR($\mathbf{r}$) over all $\mathbf{r}$ within the cube, in line with Ref. (35). [The FDA (23) and IEC (24,25) mandate averaging over cubes rather than spheres.]

Fast Region Growth

To find an N-gram cube around each $\mathbf{r}$, we use a fast algorithm rather than brute-force region growth because the latter is computationally infeasible. We first form a list of spatial positions from a simple cubic lattice in order of distance from the origin and interpret this as a "universal" list of offsets from any given position $\mathbf{r}$. We then find the set of voxels that comprise N grams of tissue around $\mathbf{r}$ by choosing the shortest prefix of this list that yields sufficient total mass. Formally, given the mass per voxel around $\mathbf{r}$ and this universal list, we form a voxel mass vector and search the cumulative sum of this voxel mass vector for the number of voxels needed to form the set; this rapidly determines the cluster of points that comprise an N-gram cube around $\mathbf{r}$. Note that for a spatial location on the edge of the head bordering air (where $\sigma_{air} = 0$), the associated $\mathbf{r}$ may not be at the center of the corresponding N-gram averaging cube, but this is mitigated by the fact that this $\mathbf{r}$ is often part of the averaging cubes of many adjacent spatial locations, as noted in Ref. (36).

Duty Cycle

When computing SAR, the effect of the trajectory acceleration factor, R, is always accounted for to ensure that any SAR differences across R reflect only the extra power needed to maintain target fidelity. For example, $R = 1$ pTX pulses (6.8 msec long) have a 100% duty cycle, whereas $R = 4$ pTX pulses (1.81 msec long) have a 26% duty cycle. This is accomplished by fixing the repetition time (TR) to 6.8 msec for each effective sequence in which the pTX pulses are used, regardless of R.

RESULTS
Birdcage Mode

We begin by driving the array in a birdcage configuration, transmitting a 2.6-ampere, 3-msec, 100%-duty-cycle rectangular pulse shape through each channel in the absence of gradients and setting the phase of channel p's pulse shape to $45(p - 1)$ degrees. This produces a 90° flip angle in the center transverse slice of the head, analogously to the "90°/3-msec" hard pulse of
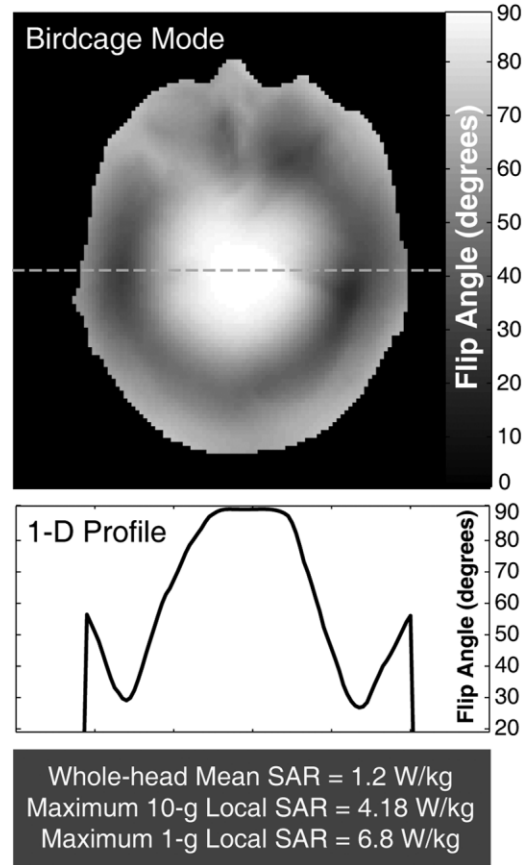
Figure 2. Birdcage mode simulation. For $p = 1, ..., 8$, transmission channel p is driven with a 3-msec, 2.6-ampere, 100%-duty-cycle rectangular pulse with phase equal to $45(p - 1)$ degrees, producing a 90° flip in the center of the head (center transverse slice shown along with 1D profile and SAR statistics). Center brightening is evident, as well as signal loss left and right of center.

Ref. (37). Figure 2 depicts the inhomogeneous flip angle map that arises in the head when the set of pulse shapes that comprise one pTX pulse undergoes Bloch-equation simulation, along with the resulting SAR values. The image exhibits strong center brightening, resembling brain images collected on actual 7T systems equipped with homogeneous RF excitation volume birdcage coils (9,10,27). In this case, there is an approximately 3-to-1 variation in peak-to-trough flip angle. The qualitative similarity of the simulated birdcage mode shown in Fig. 2 to the simulated and in vivo images presented in the lower half of the fifth figure in Ref. (10) suggests, to some extent, that the simulation methodology accurately captures the behavior of an eight-channel array at 7T.

SAR as a Function of R and θ for Fixed Excitation Quality

The top row of Fig. 3 shows the simulated square inner-volume excitations for $R = 4$, along with ϵ_1 and ϵ_{tot} error with respect to the 28×28 mm target box pattern; for all cases, $\epsilon_1 = 15 \pm 2\%$ and $\epsilon_{tot} = 40 \pm 1\%$. Figure 3 also graphs global and maximum local 1g SAR for each accel-
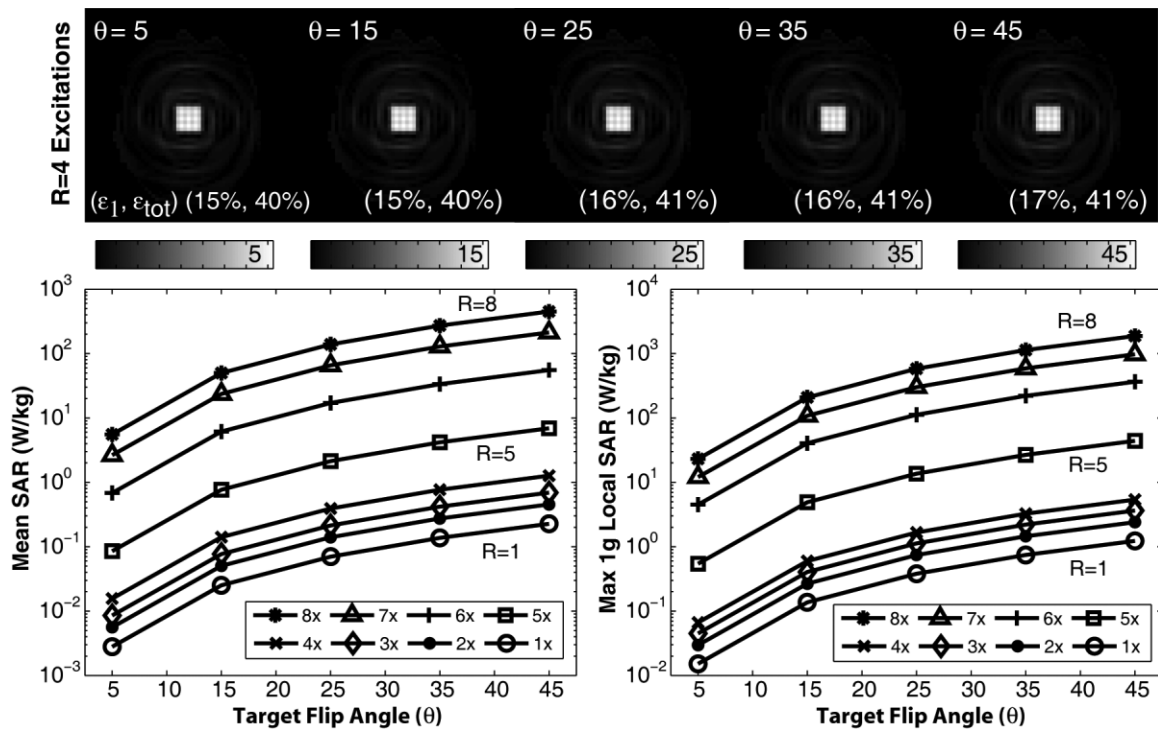
Figure 3. SAR as a function of acceleration factor, R, and flip angle, θ (fixed excitation quality). Target: 28 × 28 mm centered square with in-box flip angle θ, $\epsilon_1 = 15 \pm 2\%$, $\epsilon_{tot} = 40 \pm 1\%$. Top row: R = 4 excitations. Bottom row: mean SAR and maximum 1g SAR as a function of (R, θ). For fixed θ, SAR grows rapidly with R; for fixed R, SAR grows quadratically with θ.

eration factor (R = 1, …, 8) as a function of flip angle (θ = 5, 15, …, 45°). For fixed R, global and local SAR scale quadratically with flip angle, whereas for fixed θ, mean and local SAR increase more than quadratically with R. Finally, global and local SAR vary strikingly by over five orders of magnitude across the various excitations.

In general, the eight RF pulse shapes used to produce each of the excitations in Fig. 3 consistently exhibit low amperages during the time interval when the trajectory proceeds through high-frequency k-space regions, and progressively larger amperages as the trajectory spirals inward toward the origin of k-space. In other words, all RF pulse shapes deposit most of their energy at low spatial frequencies. For the 15° excitation, the peak RF magnitude across all eight pulse shapes increases from 1.5 amperes for R = 1, to 8 amperes for R = 4, to 150 amperes for R = 7. The R = 7 pulse shape has a much higher peak than the R = 1 pulse shape, a natural consequence of the fact that with only an R = 7 spiral, there are very few degrees of freedom in k-space with which to form the excitation (relative to the Nyquist-sampled R = 1 spiral), forcing the algorithm to drive the channel profiles intensely with high-amplitude RF pulse shapes in order to form the desired pattern. This lack of k-space freedom forces the system to rely heavily on its degrees of freedom in the spatial domain and partly explains the high SAR values of the highly accelerated pTX pulses.

Maximum Local SAR as a Function of R for Fixed Mean SAR and Excitation Quality

Since MR scanners typically monitor mean SAR (in the form of average forward power), it is informative to as-

sess local SAR under the condition where the operator adjusts the sequence to achieve a fixed global average SAR. Figure 4 depicts such a scenario, showing iso-SAR operating contours in the (R, θ) parameter space that characterize how maximum local 1g and 10g SAR vary when mean SAR is held constant at 0.15 W/kg. Excitation patterns and residual errors here are the same as in Fig. 3. Figure 4 shows that maximum local 1g SAR is always higher than maximum local 10g SAR, which in turn is always higher than whole-head mean SAR. Across R, local 1g and 10g SAR vary from peak-to-trough by factors of 1.64 and 1.34, respectively. Furthermore, Fig. 4's left panel shows that in order to produce fixed-fidelity excitations with 0.15 W/kg mean SAR, in-box flip angle must decrease rapidly with R, e.g., only a 2° flip is achievable for R = 6, whereas a 36° flip is possible using an unaccelerated trajectory. Counterintuitively, Fig. 4's right panel reveals that maximum local 1g and 10g SAR are not monotonic with R, e.g., the R = 4 excitation produces 1.3 times less maximum local SAR than the R = 1 excitation. Finally, the ratios of local 1g and 10g SAR to mean SAR are erratic: they are roughly constant for R = 1 to 3, decrease for R = 4, rise for R = 5, 6, and then decrease again for R = 7, 8.

SAR as a Function of R and Spatial Position of the Excitation

To assess the effect of excitation symmetry on SAR we design pTX pulses that excite 28 × 28 mm, 15° flip angle squares at different locations along the right–left (RL, or "x") axis and the anterior–posterior (AP, or "y") axis. Excitation quality is fixed across all designs. Fig-

Figure 4. Local SAR and θ as a function of R (fixed mean SAR and excitation quality). Target: 28 × 28 mm centered square with $\epsilon_1 = 15 \pm 2\%$ and $\epsilon_{tot} = 40 \pm 1\%$. For each R, target flip angle, θ, is varied until mean SAR = 0.15 ± 0.01 W/kg. Left: to achieve fixed mean SAR, θ must decrease radically with R. Only a 2° flip is achievable for $R = 6$, whereas a 36° flip is achievable using an $R = 1$ unaccelerated trajectory. Right: maximum 1g and 10g SAR are not monotonic with R, eg, the $R = 4$ excitation has 1.3 times lower local SAR than the $R = 1$ one.
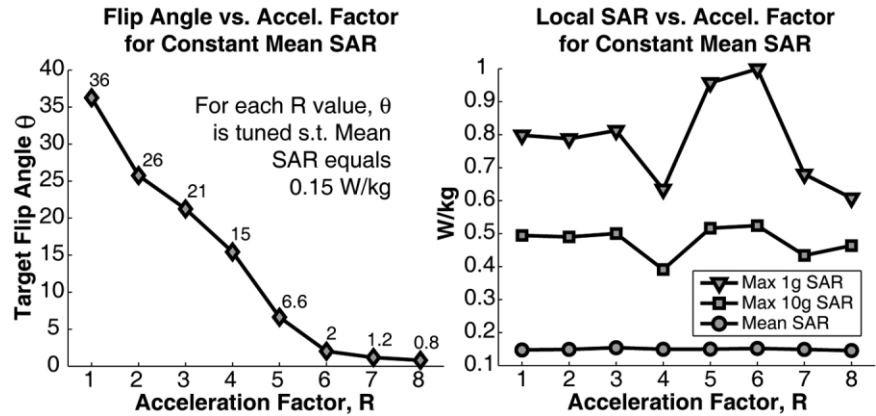
ure 5 illustrates how global and maximum local 1g SAR behave when exciting boxes centered at different x locations. The upper row depicts $R = 4$ excitations, while the next two rows show local 1g SAR maps arising due to $R = 1$ and $R = 5$ excitations. For a given row of local SAR maps, all are displayed using the same dynamic range, permitting local SAR comparisons among the maps of each row. Furthermore, because a 1g local SAR datapoint exists for each of the voxels in the 3D head model, the 2D local SAR maps have been "collapsed" along the z-axis. Namely, for each location (x, y) in each given map, we have displayed $\max_z \text{SAR}_{\text{1-gram}}(x, y, z)$. Finally, the bottom row of Fig. 5 illustrates log-scaled plots of mean SAR and maximum local 1g SAR as a function of box position. Figure 6 shows SAR behavior versus box shift along y and is formatted analogously to Fig. 5, except here local SAR maps are not displayed.

In both Figs. 5 and 6, SAR as a function of position is roughly convex for low trajectory acceleration factors ($R = 1$ to 4), i.e., centered excitation boxes yield the lowest SAR. At higher acceleration factors, however, centered excitations generally produce the highest SAR. Figure 5 also shows that mean and local SAR do not always behave similarly, e.g., for $R \le 4$, the mean SAR vs. R curves are generally symmetric about $x_0 = 0$, whereas the local SAR curves are asymmetric. Figure 6 shows that qualitative SAR differences also arise when shifting the box along y. Furthermore, for fixed R, all of Fig. 6's local and mean SAR curves seem to exhibit the same shape, in contrast with the $R \le 4$ curves of Fig. 5.

Regarding the local SAR maps of Fig. 5, the local 1g SAR patterns for $R = 1$ change across space in a way that is correlated with the position of the excited box, while the $R = 5$ local SAR maps, to the first order, seem to only scale by a multiplicative constant with box position. Finally, the peaks in both the $R = 1$ and $R = 5$ local SAR maps are not strongly correlated with the box position.

SAR as a Function of R and In-Box NRMSE, ϵ_1, for Fixed Overall NRMSE, ϵ_{tot}

Figure 7 shows the effect of excitation quality on SAR, illustrating global and maximum local 1g SAR for $R = 1$, ..., 8 due to exciting 28 × 28 mm centered boxes with different in-box fidelities; ϵ_1 varies from 10%, 15%, ..., 30%, while ϵ_{tot} is fixed at 40 ± 2%. Figure 7's top row shows excitation patterns associated with $R = 4$, while

the bottom row shows global and maximum local 1g SAR as a function of ϵ_1. We see from the top row of $R = 4$ excitations that the in-box flip angle decreases (the boxes grow darker) as more in-box error is permitted. Further, global SAR and maximum local 1g SAR both increase rapidly with R, ranging over three orders of magnitude for each fixed ϵ_1. Finally, SAR decreases fairly regularly with ϵ_1 for most accelerations, but this does not hold for $R = 5$ and $R = 6$, eg, when $R = 6$, the $\epsilon_1 = 15\%$ excitation produces 1.3 and 1.5 times *higher* mean and local SAR than the $\epsilon_1 = 10\%$ excitation.

SAR as a Function of R and ϵ_{tot} for Fixed ϵ_1

Figure 8 illustrates the dual of Fig. 7's experiment, showing how global and maximum local 1g SAR behave across R when producing excitations with different overall fidelities ($\epsilon_{tot} = 20\%$, 25%, ..., 40%) while keeping $\epsilon_1 = 15 \pm 1\%$. Here, global SAR and local SAR vary by over four orders of magnitude across R and ϵ_{tot}. For $R \ne 5$, global and local SAR decrease monotonically with ϵ_{tot}, and even for $R = 5$, SAR is nearly monotonic: the lower-fidelity $\epsilon_{tot} = 35\%$ excitation produces only 1.007 times higher SAR than the $\epsilon_{tot} = 30\%$ case. (Note: there are no datapoints for $\epsilon_{tot} = 20\%$ when $R = 7$ and $R = 8$ because for these cases the pTX pulse design algorithm does not produce well-conditioned solutions.)

SAR vs. R and Box Orientation

Figure 9 illustrates the effect of excitation orientation on global and maximum local 1g SAR across the eight acceleration factors. Here we excite 44 × 28 mm rectangles in the center of the head that are rotated by ψ degrees, characterizing SAR as a function of R and ψ. Excitation fidelity is fixed as in prior experiments. For $R \le 4$, SAR is relatively constant, whereas for $R > 4$, SAR exhibits spikes at particular rotations. For example, when $R = 5$, exciting a 90°-rotated box produces 3.3 W/kg of maximum local 1g SAR, whereas exciting a 135°-rotated box produces 9.54 W/kg, i.e., local SAR varies by a factor of 2.9 when simply rotating the excitation by 45°, even with acceleration factor and excitation quality held constant. Finally, SAR is generally higher when boxes are highly asymmetric with respect to the AP-direction (y-axis) of the head (consider the $R = 6$, ψ = 45° excitation).
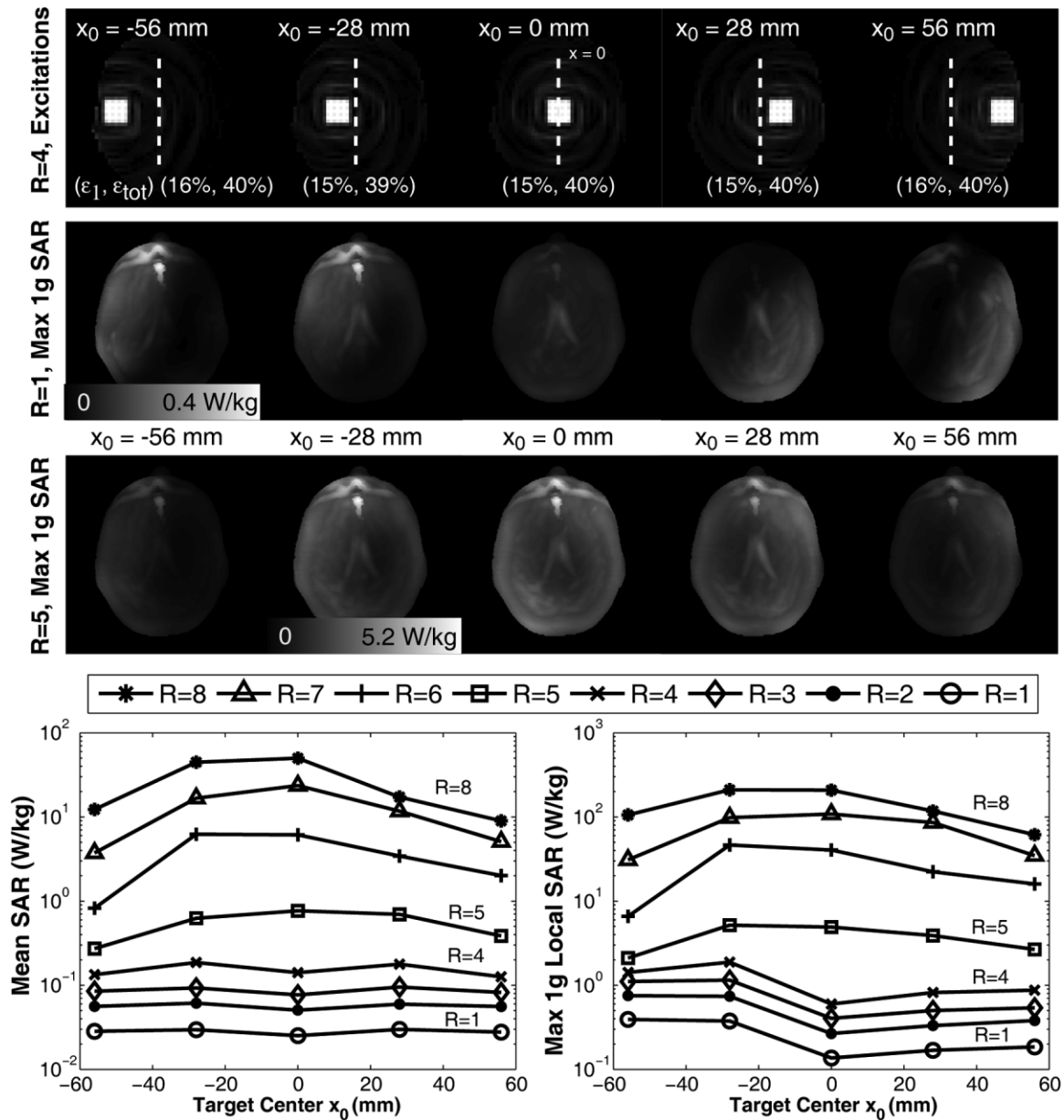
Figure 5. SAR as a function of R and shift along x (fixed excitation quality). Target: $15°$, 28×28 mm square whose center x_0 varies along x with $\epsilon_1 = 15 \pm 1\%$ and $\epsilon_{tot} = 40 \pm 1\%$. Top row: $R = 4$ excitations. Second and third rows: local 1g SAR maps due to $R = 1$ and $R = 5$ pulses. Each spatial location (x, y) shown equals $\max_z \text{SAR}_{1\text{-gram}}(x, y, z)$, i.e., the maps have been collapsed along the z axis to efficiently display 3D spatial SAR data. Bottom row: mean SAR and maximum 1g SAR as a function of (R, x_0). For $R \leq 4$, SAR increases as $|x_0|$ increases, whereas for $R > 4$, SAR decreases. For $R = 1$, local SAR seems to vary strongly across space with excitation position, whereas for $R = 5$, it seems to scale by only a multiplicative constant.

SAR vs. R and Box Size

Figure 10 illustrates how the size of an excitation impacts global and maximum local 1g SAR. Here a series of increasingly larger boxes of length and width N (mm) are excited across various acceleration factors. Excitation fidelity is fixed as in prior experiments, and Fig. 10 is formatted analogously to Figs. 6–9. Both the log-scaled and normalized data along the middle and bottom rows of Fig. 10 show that mean and local SAR behave quite differently depending on R: for $R \leq 4$, SAR grows rapidly with N, whereas for $R > 4$, SAR decreases with N. This means that for highly accelerated trajecto-

ries, exciting larger regions actually reduces energy deposition. For example, for $R = 5$, exciting a 52 mm box produces 3.2 times less mean SAR than exciting a 12 mm box, yet for $R = 1$ the opposite behavior occurs: exciting a 52 mm rather than 12 mm box leads to 10 times higher mean SAR.

SAR vs. R and Box Smoothness

Figure 11 shows how sharp excitation pattern edges affect SAR. Here, increasingly smooth 44×44 mm centered boxes are excited and the SAR of each is ana-
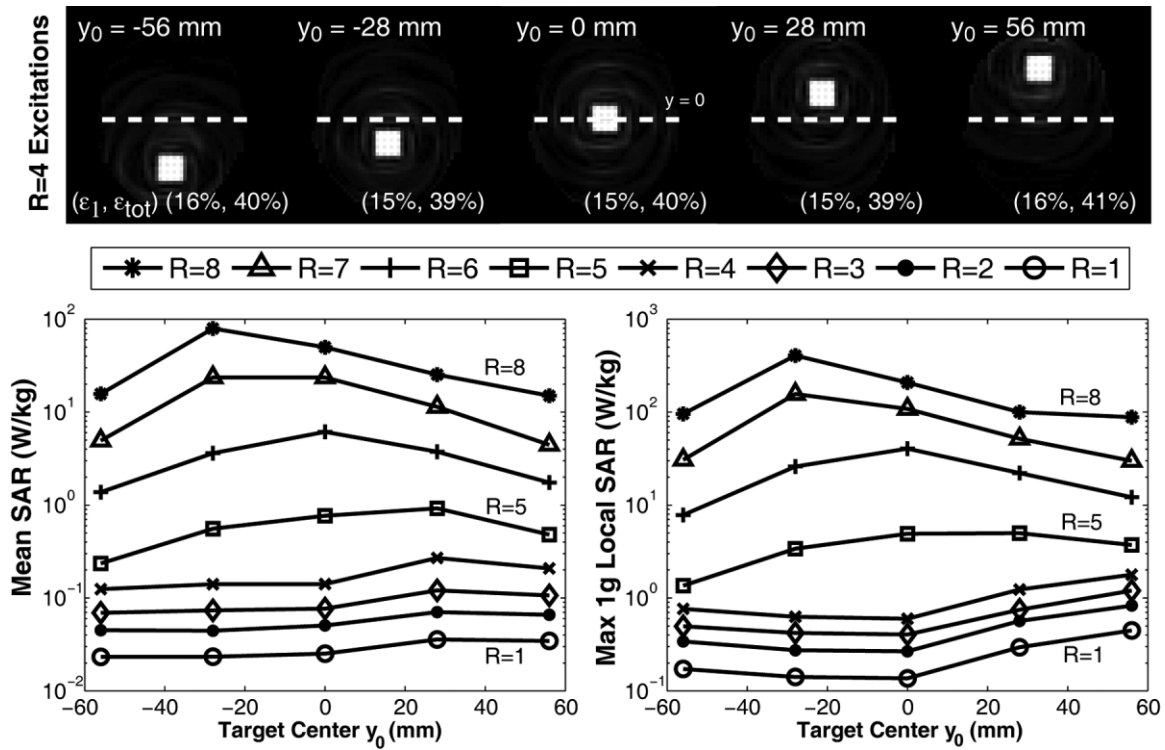
Figure 6. SAR as a function of R and shift along y (fixed excitation quality). Target: $15°$, 28×28 mm square whose center y_0 varies along y with $\epsilon_1 = 15 \pm 1\%$ and $\epsilon_{tot} = 40 \pm 1\%$. Top row: $R = 4$ excitations. Bottom row: mean SAR and maximum 1g SAR as a function of (R, y_0).
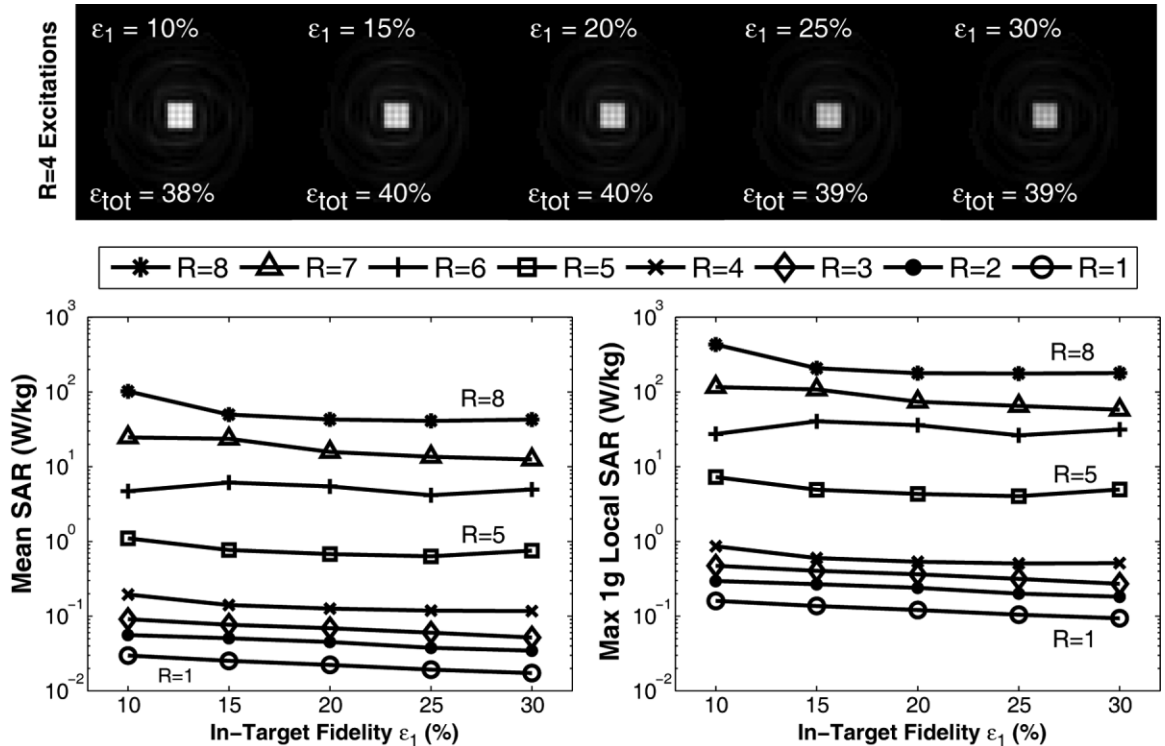
Figure 7. SAR as a function of R and ϵ_1 (fixed ϵ_{tot}). Target: $15°$, 28×28 mm square with varying ϵ_1 and $\epsilon_{tot} = 40 \pm 2\%$. Top row: $R = 4$ excitations; in-box flip angle decreases with ϵ_1. Bottom row: mean SAR and maximum 1g SAR as a function of (R, ϵ_1). For $R \neq 6$, SAR decreases fairly regularly with ϵ_1. For $R = 6$, SAR is actually higher when $\epsilon_1 = 15\%$ than when $\epsilon_1 = 10\%$.
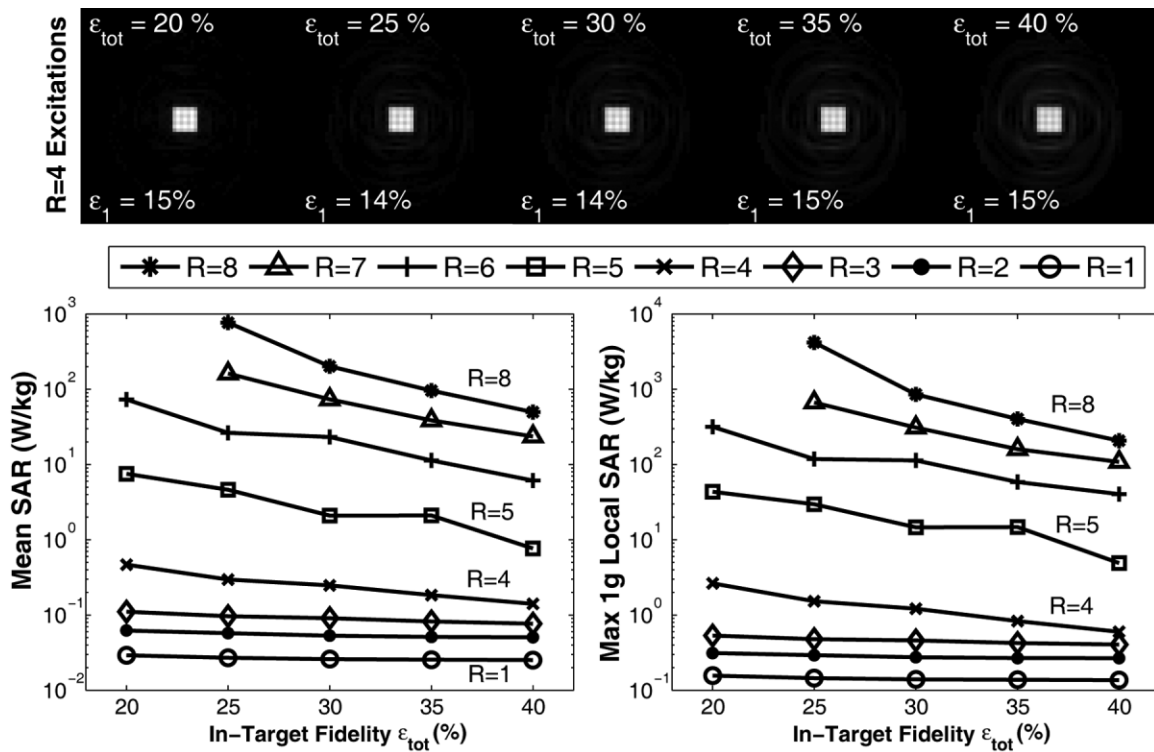
Figure 8. SAR as a function of R and ϵ_{tot} (fixed ϵ_1). Target: 15°, 28 × 28 mm centered square with varying ϵ_{tot} and $\epsilon_1 = 15 \pm 1\%$. Top row: $R = 4$ excitations. Outside of the square, artifacts increase with ϵ_{tot}. Bottom row: mean SAR and maximum 1g SAR as a function of (R, ϵ_{tot}). For all R, SAR generally decreases smoothly with ϵ_{tot}.

lyzed. The series of desired excitations is generated by applying successively larger $M \times M$ mm Gaussian smoothing kernels to the original sharp-edged target pattern and running the design algorithm each time to produce a pTX pulse. The top row of Fig. 11 shows that for $R = 4$ the excitations increase in smoothness with M as intended. The bottom row shows that mean and local SAR decrease significantly with target smoothness for all R. For example, when $R = 6$, exciting the smoothest box requires 2.8 times less global SAR and 2.7 times less maximum local 1g SAR than does exciting the sharpest-edged box.

Mean vs. Maximum Local 1g and 10g SAR

Across all experiments, maximum 1g SAR ranges from 3.8 to 13.8 times larger than corresponding mean SAR and on average is 5.6 times larger. Likewise, maximum 10g SAR is always 2.3 to 7.7 times larger than mean SAR and on average is 3.4 times larger. Finally, maximum 1g SAR ranges from 1.1 to 2.1 times larger than maximum 10g SAR and on average is 1.7 times larger.

DISCUSSION
Model Resolution

The high-resolution head model in this study meets or exceeds the requirements for accurate SAR calculation in volumes as small as 1g because each of its voxels contains no more than 0.0037 g of tissue (every possible 1g region consists of at least 270 cells). Additionally, the model's high resolution mitigates staircasing arti-

facts (38) that adversely impact local field and local SAR calculations because the model's $\approx$1000 cells per 300-MHz wavelength should reduce staircase error to less than 1 db (39).

Comparisons Across Experiments

Considerable effort has been made to keep excitation fidelity constant across all experiments and thus permit SAR comparisons across experiments. One noticeable trend is that a consistent "jump" in mean and local SAR occurs as R transitions from 4 to 5, regardless of excitation shape, size, asymmetry, etc, which suggests the array is better conditioned in the $R \leq 4$ operating region.

Cost of Trajectory Acceleration

Across all experiments, global and local SAR always increase dramatically with trajectory acceleration factor. Highly accelerated pulses yield extremely high SAR values and may not be practical for in vivo imaging. Furthermore, because even moderate trajectory accelerations may lead to order-of-magnitude SAR increases, it seems likely that further innovation beyond or in conjunction with conventional pTX pulse design is necessary in order to enable the use of highly accelerated trajectories. Two recent examples of design innovation are the emerging body of algorithms that explicitly consider SAR during the design of parallel transmission pulses and multichannel arrays (40–46) and the recent proposal of several methods that moni-
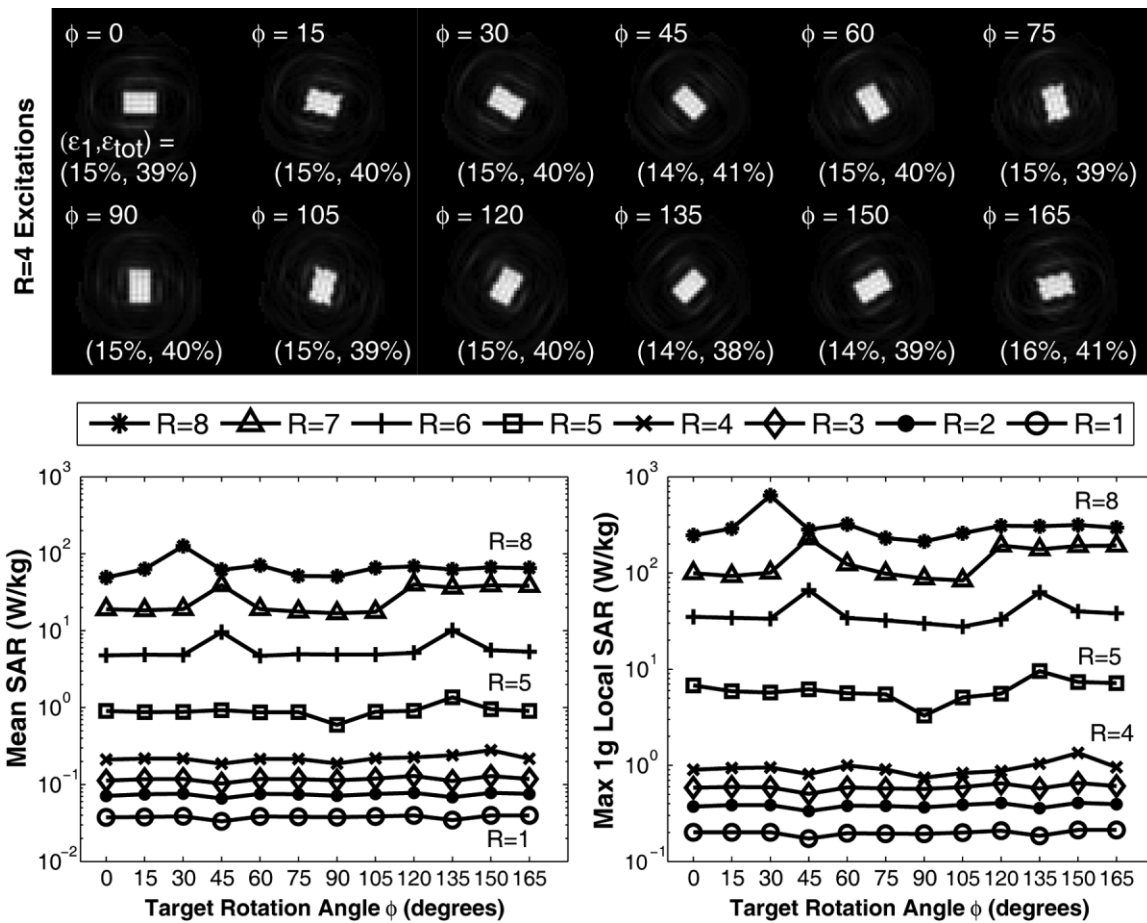
Figure 9. SAR as a function of R and target rotation angle ψ (fixed excitation quality). Target: 15°, 44×28 mm centered rectangle with varying ψ, with $\epsilon_1 = 15 \pm 1\%$ and $\epsilon_{tot} = 40 \pm 2\%$. Top row: $R = 4$ excitations. Bottom row: mean SAR and maximum 1g SAR as a function of (R, ψ). For $R \leq 4$, SAR is relatively constant, whereas for $R > 4$, SAR varies.

tor and track SAR arising during a scan in real time (47,48). One limitation that seems unavoidable from a design standpoint, however, is that in order to minimize or guarantee local SAR at a particular spatial location during the design stage, one must place a quadratic constraint on the system of equations being solved (41,46). For example, the algorithm of Ref. (41) explicitly accounts for global SAR as well as local SAR at a few other locations by incorporating several quadratic constraints into the design. But in order to design truly SAR-optimal pulses—ones where local SAR is guaranteed at all spatial locations—one is faced with the computationally-intractable problem of solving a system of equations with millions of quadratic constraints. Finally, one may be able to mitigate SAR by taking a hardware approach, improving the efficiency and spatial encoding capabilities of pTX arrays (49,50).

SAR Observations

In Fig. 3, mean and local SAR scale quadratically with flip angle. Figure 4 shows that the ratio of local to mean SAR does not increase monotonically with acceleration factor. Figures 5 and 6 show that mean and local SAR behave nonintuitively when excitation spatial position is varied. For $R = 1$, local SAR varies significantly

across space with excitation position, whereas for $R = 5$, to the first order, the local SAR maps simply undergo scalings by a multiplicative constant. Figure 7 shows that it is not always possible to reduce SAR by simply permitting more excitation error within a specific spatial region (e.g., within the box) and that one may in fact significantly increase SAR (e.g., by a factor of 1.5) by generating lower-quality excitations. Figure 8, on the other hand, shows that permitting more overall excitation pattern error generally decreases SAR. Figure 9 shows that for large acceleration factors, excitation asymmetry detrimentally impacts SAR. Figure 10 shows that SAR is sensitive to excitation size, suggesting that parallel transmission may complicate the ability to perform and flexibly scale reduced-FOV imaging (19). Finally, Fig. 11 suggests that sharp edges are costly in terms of SAR, revealing that one reliable way to reduce SAR is to excite a smoother version of the desired pattern.

CONCLUSION

In conclusion, with the exception of dramatic SAR increases with trajectory acceleration factor, global and local SAR do not always exhibit intuitive trends. None-
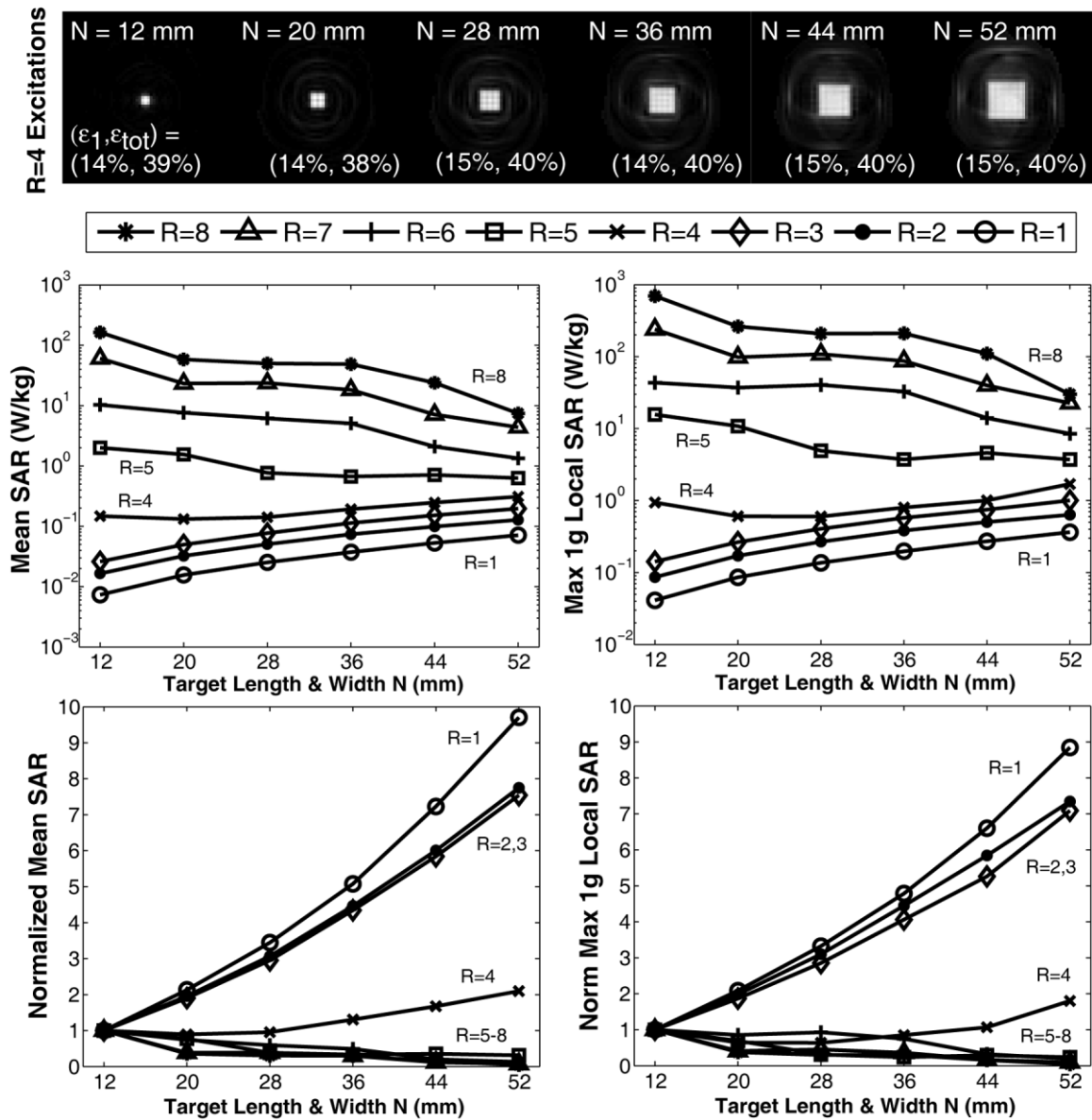
Figure 10. SAR as a function of R and target size N (fixed excitation quality). Target: $15°$ centered square of varying size with $\epsilon_1 = 15 \pm 1\%$ and $\epsilon_{tot} = 40 \pm 2\%$. Top row: $R = 4$ excitations. Middle row: mean SAR and maximum 1g SAR as a function of (R, N). Bottom row: for each R, data from middle row is scaled so that SAR$(R, N = 12$ mm$)$ is unity. For $R \leq 4$, SAR increases rapidly with N, whereas for $R > 4$, exciting larger regions reduces energy deposition.

theless, it is clear from the experiments that maximum local 1g and 10g SAR are always significantly higher than global SAR. Because both the United States and European Union safety standards impose limits on maximum local SAR (23–25), and because the ratio of local to global SAR is often considerably greater than the regulatory ratio required to maintain safety compliance for the human head by monitoring average power alone, it is evident that local SAR, rather than global SAR, is the limiting factor of eight-channel parallel transmission at 7T. Namely, it is likely that the safety limit imposed upon local SAR will preclude the user from utilizing the full limit of mean SAR. Seifert et al. (31) arrived at this identical conclusion after studying four-channel parallel transmission at 3T.

Although the range of excitation patterns studied here is not exhaustive, a sufficient number of variations of the size, shape, position, rotation, and smoothness of the excitation pattern have been considered to suggest that mean and local SAR exhibit complex and at times nonintuitive behavior as a function of target excitation pattern and trajectory acceleration factor. In order to ensure patient safety, it seems that model-based validation of individual target patterns and corresponding sets of parallel transmission pulses will be required.
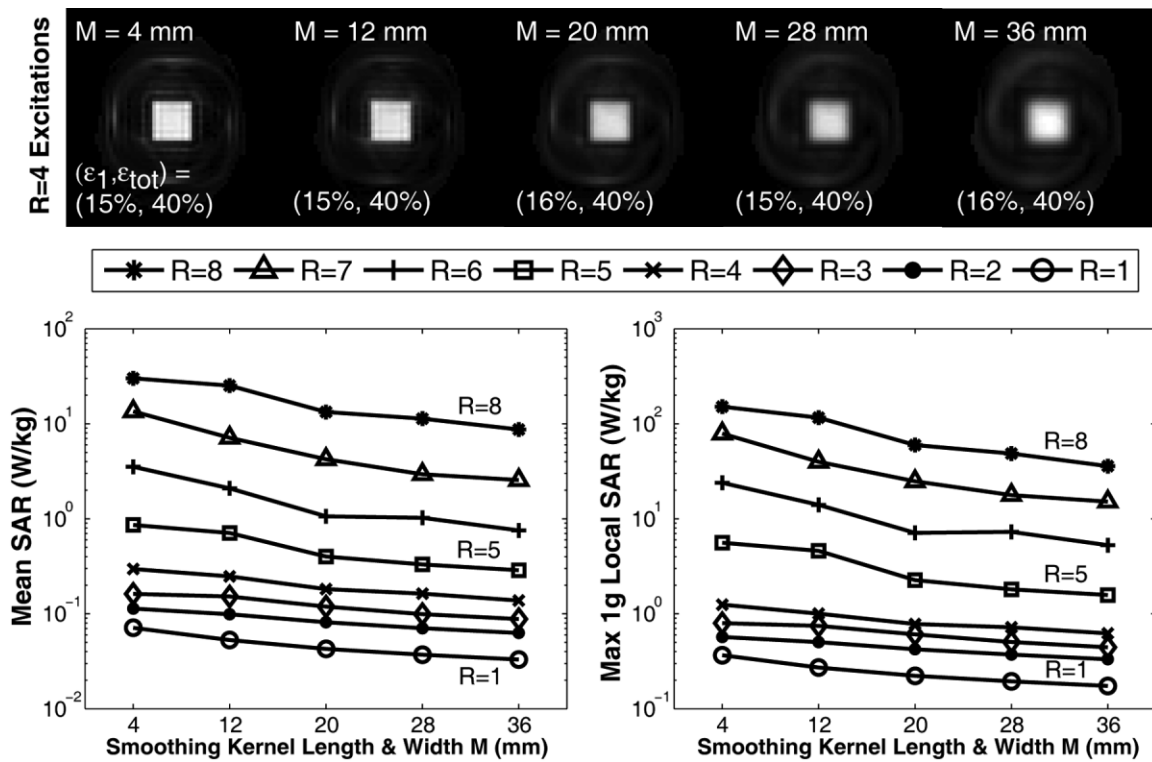
Figure 11. SAR as a function of *R* and target smoothness (fixed excitation quality). Target: 15°, 44 × 44 mm square smoothed with various *M* × *M* mm Gaussian kernels with $\epsilon_1 = 15 \pm 1\%$ and $\epsilon_{tot} = 40 \pm 1\%$. The base case of no smoothing is when *M* = 4 mm (pixel resolution is 4 mm, so an *M* = 4 mm window is simply a one-pixel unit-energy kernel). Top row: *R* = 4 excitations. Bottom row: mean SAR and maximum 1g SAR as a function of (*R, M*). In general, SAR generally decreases smoothly with M.

REFERENCES

1. Graesslin I, Vernickel P, Schmidt J, et al. Whole body 3T MRI system with eight parallel RF transmission channels. In: Proc 14th Annual Meeting ISMRM, Seattle, 2006. Abstract 129.
2. Katscher U, Bornert P, Leussler C, van den Brink JS. Transmit SENSE. Magn Reson Med 2003;49:144–150.
3. Setsompop K, Wald LL, Alagappan V, et al. Parallel RF transmission with 8 channels at 3 Tesla. Magn Reson Med 2006;56:1163–1171.
4. Ullmann P, Junge S, Wick M, Seifert F, Ruhm W, Hennig J. Experimental analysis of parallel excitation using dedicated coil setups and simultaneous RF transmission on multiple channels. Magn Reson Med 2005;54:994–1001.
5. Zhu Y. Parallel excitation with an array of transmit coils. Magn Reson Med 2004;51:775–784.
6. Feinberg DA, Hoenninger JC, Crooks LE, Kaufman L, Watts JC, Arakawa M. Inner volume MR imaging: technical concepts and their application. Radiology 1985;156:743–747.
7. Bottomley P, Andrews E. RF magnetic field penetration, phase shift and power dissipation in biological tissue: implications for NMR imaging. Phys Med Biol 1978;23:630–643.
8. Bomsdorf H, Helzel T, Kunz D, Roschmann P, Tschendel O, Wieland J. Spectroscopy and imaging with a 4 Tesla whole-body MR system. NMR Biomed 1988;1:151–158.
9. Van de Moortele P-F, Akgun C, Adriany G, et al. B_1 destructive interference and spatial phase patterns at 7T with a head transceiver array coil. Magn Reson Med 2005;54:1503–1518.
10. Vaughan JT, Garwood M, Collins CM, et al. 7T vs. 4T: RF power, homogeneity, and signal-to-noise comparison in head images. Magn Reson Med 2001;46:24–30.
11. Collins CM, Wanzhan L, Schreiber W, Yang QX, Smith MB. Central brightening due to constructive interference with, without, and despite dielectric resonance. J Magn Reson Imag 2005;21:192–196.
12. Pauly J, Nishimura D, Macovski A. A k-space analysis of small-tip angle excitation. J Magn Reson 1989;81:43–56.
13. Pruessman KP, Weiger M, Scheidegger MB, Boesiger P. SENSE: sensitivity encoding for fast MRI. Magn Reson Med 1999;42:952–962.
14. Sodickson DK, Manning WJ. Simultaneous acquisition of spatial harmonics (SMASH): fast imaging with radiofrequency coil arrays. Magn Reson Med 1997;38:591–603.
15. Graesslin I, Falaggis K, Biederer S, et al. SAR simulations and experiments for parallel transmission. In: Proc 15th Annual Meeting ISMRM, Berlin, 2007. Abstract 1090.
16. Katscher U, Vernickel P, Overweg J. Basics of RF power behaviour in parallel transmission. In: Proc 13th Annual Meeting ISMRM, Miami, 2005. Abstract 17.
17. Wu X, Akgun C, Vaughan JT, Ugurbil K, Van de Moortele P-F. SAR analysis for transmit SENSE at 7T with a human head model. In: Proceedings 15th Annual Meeting ISMRM, Berlin, 2007. Abstract 3350.
18. Katscher U, Bornert P. Parallel RF transmission in MRI. NMR Biomed 2006;19:393–400.
19. Hu X, Parrish T. Reduction of field of view for dynamic imaging. Magn Reson Med 1994;31:691–694.
20. van der Zwaag W, Francis S, Bowtell R. Improved echo volumar imaging (EVI) for functional MRI. Magn Reson Med 2006;56:1320–1327.
21. Yang Y, Mattay VS, Weinberger DR, Frank JA, Duyn JH. Localized echo-volume imaging methods for functional MRI. J Magn Reson Imag 1997;7:371–375.
22. Davies NP, Jezzard P. Selective arterial spin labeling (SASL): Perfusion territory mapping of selected feeding arteries tagged using two-dimensional radiofrequency pulses. Magn Reson Med 2003;49:1133–1142.
23. Center for Devices and Radiologic Health. Guidance for the submission of premarket notifications for magnetic resonance diagnostic devices. Rockville, MD: Food and Drug Administration; 1998.
24. International Electrotechnical Commission. International standard, medical equipment—part 2: particular requirements for the safety of magnetic resonance equipment for medical diagnosis, 2nd revision. Geneva: International Electrotechnical Commission; 2002. p 29–31.

25. IEC Standard 60601-2-33. Particular requirements for the safety of magnetic resonance equipment for medical diagnosis. Chicago: International Electrotechnical Commission; 2004.

26. Kunz KS, Luebbers RJ. The finite difference time domain method for electromagnetics. Boca Raton, FL: CRC Press; 1993.

27. Angelone LM, Tulloch S, Wiggins G, Iwaki S, Makris N, Bonmassar G. New high resolution head model for accurate electromagnetic field computation. In: Proc 13th Annual Meeting ISMRM, Miami, 2005. Abstract 881.

28. Angelone LM, Makris N, Vasios CE, Wald LL, Bonmassar G. Effect of transmit array phase relationship on local specific absorption rate (SAR). In: Proc 14th Annual Meeting ISMRM, Seattle, 2006. Abstract 2038.

29. Yee KS. Numerical solutions of initial boundary value problems involving Maxwell's equations in isotropic media. IEEE Trans Antenn Propag 1966;AP-14:302–307.

30. Mao W, Wang Z, Smith MB, Collins CM. Calculation of SAR for transmit coil arrays. Concepts Magn Reson 2007;31B:127–131.

31. Seifert F, Wubbeler G, Junge S, Ittermann B, Rinneberg H. Patient safety concept for multichannel transmit coils. J Magn Reson Imaging 2007;26:1315–1321.

32. Hoult DI. The principle of reciprocity in signal strength calculations — a mathematical guide. Concepts Magn Reson 2000;12:173–187.

33. Grissom WA, Yip CY, Zhang Z, Stenger VA, Fessler JA, Noll DC. Spatial domain method for the design of RF pulses in multicoil parallel excitation. Magn Reson Med 2006;56:620–629.

34. Bloch F. Nuclear induction. Phys Rev A 1946;70:460–474.

35. IEEE C95.3-2002. Recommended practice for measurements and computations of radio frequency electromagnetic fields with respect to human exposure to such fields, 100 kHz-300 GHz; 2002.

36. Angelone LM, Potthast A, Segonne F, Iwaki S, Belliveau JW, Giorgio B. Metallic electrodes and leads in simultaneous EEG-MRI: specific absorption rate (SAR) simulation studies. Bioelectromagnetics 2004;25:285–295.

37. Collins CM, Smith MB. Signal-to-noise ratio and absorbed power as functions of main magnetic field strength, and definition of "90 degrees" RF pulse for the head in the birdcage coil. Magn Reson Med 2001;45:684–691.

38. Cangellaris AC, Wright DB. Analysis of the numerical error caused by the stair-stepped approximation of a conducting boundary in FDTD simulations of electromagnetic phenomena. IEEE Trans Antenn Propag 1991;39:1518–1525.

39. Holland R, Cable VP, Wilson LC. Finite-volume time-domain (FVTD) techniques for EM scattering. IEEE Trans Electromagn Compat 1991;33:281–294.

40. Graesslin I, Biederer S, Schweser F, Zimmermann K-H, Katscher U, Bornert P. SAR reduction for parallel transmission using VERSE and k-space filtering. In: Proc 15th Annual Meeting ISMRM, Berlin, 2007. Abstract 674.

41. Graesslin I, Schweser F, Annighoefer B, et al. A minimum SAR RF pulse design approach for parallel Tx with local hot spot suppression and exact fidelity constraint. In: Proc 16th Annual Meeting ISMRM, Toronto, 2008. Abstract 621.

42. Ibrahim TS, Tang L. A whole-body 7 Tesla RF excitation scheme with much improved B1+ field homogeneity and local/global SARs over quadrature excitation. In: Proc 15th Annual Meeting ISMRM, Berlin, 2007. Abstract 1013.

43. Van den Berg CAT, van den Bergen B, Van de Kramer JB, et al. Simultaneous B_1^+ Homogenization and specific absorption rate hotspot suppression using a magnetic resonance phased array transmit coil. Magn Reson Med 2007;57:577–586.

44. Wang Z, Oh S-H, Smith MB, Collins CM. RF shimming considering both excitation homogeneity and SAR. In: Proc 15th Annual Meeting ISMRM, Berlin, 2007. Abstract 1022.

45. Wu X, Akgun C, Vaughan JT, Ugurbil K, Van de Moortele P-F. SAR reduction in transmit SENSE using adapted excitation k-space trajectories. In: Proc 15th Annual Meeting ISMRM, Berlin, 2007. Abstract 673.

46. Zelinski AC, Goyal VK, Angelone LM, Bonmassar G, Wald LL, Adalsteinsson E. Designing RF pulses with optimal specific absorption rate (SAR) characteristics and exploring excitation fidelity, SAR, and pulse duration tradeoffs. In: Proc 15th Annual Meeting ISMRM, Berlin, 2007. Abstract 1699.

47. Collins CM, Wang Z, Smith MB. A conservative method for ensuring safety within transmit arrays. In: Proc 15th Annual Meeting ISMRM, Berlin, 2007. Abstract 1092.

48. Graesslin I, Biederer S, Falaggis K, et al. Real-time SAR monitoring to ensure patient safety for parallel transmission systems. In: Proc 15th Annual Meeting ISMRM, Berlin, 2007. Abstract 1086.

49. Alagappan V, Nistler J, Adalsteinsson E, et al. Degenerate mode band-pass birdcage coil for accelerated parallel excitation. Magn Reson Med 2007;57:1148–1158.

50. Alagappan V, Setsompop K, Polimeni JR, et al. Mode compression of transmit and receive arrays for parallel imaging at 7T. In: Proc 16th Annual Meeting ISMRM, Toronto, 2008. Abstract 619.